Bulletin of Geophysics and Oceanography Vol. XX, n. X, pp. XXX-XXX; Xxxxx 20xx
DOI 10.4430/bgo00544

Scattering and intrinsic attenuation in a building and the shallow subsoil: a depth-dependent analysis

M.T. Salilih[1,2], S. Parolai[2,3] and V. Poggi[1,4]

[1] *National Institute of Oceanography and Applied Geophysics – OGS, Trieste, Italy*
[2] *The Abdus Salam International Centre for Theoretical Physics (ICTP), Trieste, Italy*
[3] *University of Trieste, Trieste, Italy*
[4] *Department of Civil Engineering and Architecture, University of Pavia, Pavia, Italy*

(Received: 13 November 2025; accepted: 28 July 2026; published online: 12 November 2026)

ABSTRACT Seismic attenuation strongly influences ground motion and structural response. Intrinsic (Q_i) and scattering (Q_{sc}) attenuation parameters were estimated using an adapted multiple lapse time window analysis (MLTWA) applied to S-wave and coda-energy recordings from vertical seismic arrays installed in a 16-story reinforced-concrete building and co-located boreholes. Analytical and numerical radiative-transfer solutions were fitted to the observed normalised energy integrals using a hybrid inversion combining coarse grid search with simulated annealing. The inversion was performed at each frequency to estimate depth-dependent attenuation for three domains: the building, the shallow near surface (0–50 m), and the underlying half-space (> 50 m). Attenuation parameters were expressed as empirical power-law relations, $Q(f) = Q_0 f^n$ for each domain. The results show that attenuation is generally stronger in the near-surface layer than in the building across most of the analysed frequency ranges, whereas the building response modifies the incoming wavefield through frequency-dependent energy redistribution. The half-space exhibits higher Q values and nearly constant behaviour. Because the classical MLTWA assumptions are not fully satisfied within the building, the estimated Q_{sc} values are interpreted as apparent attenuation parameters reflecting scattering, structural reverberation, and radiation damping. These depth-dependent attenuation estimates provide valuable input for improved site-response and seismic-hazard modelling.

Key words: seismic coda, intrinsic absorption, seismic scattering, multiple lapse time window analysis (MLTWA), simulated annealing, grid search.

1. Introduction

Seismic attenuation, comprising intrinsic absorption and scattering, controls amplitude decay and influences site response and structural damage during earthquakes. The attenuation is commonly expressed in terms of quality factor Q, which quantifies the efficiency of energy propagation through the medium. A high Q indicates weak attenuation, while a low Q corresponds to strong energy loss. The inverse of the quality factor, Q^{-1}, is, therefore, a direct measure of attenuation. Reliable, frequency-dependent estimates of intrinsic (Q_i), scattering (Q_{sc}), and total (Q_s) quality factors are therefore essential for wave-propagation modelling, site-response analysis, and seismic-hazard assessment (Akinci *et al.*, 2022).

Intrinsic seismic attenuation (Q_i^{-1}) is an anelastic behaviour of a medium that irreversibly converts seismic energy into heat; it reflects mechanisms such as shear deformation, pore-fluid

© 2026 - The Author(s)

movement, and micro-crack sliding (O'Connell and Budiansky, 1977). In structural dynamics, energy dissipation is commonly described by the modal damping ratio, which is related to the modal quality factor under lightly damped conditions. Scattering attenuation, in contrast, redistributes seismic energy through elastic interactions with heterogeneities (Rachman *et al.*, 2017). Separating intrinsic and scattering attenuation is, therefore, important because the same observed energy decay may result from either true material dissipation or wavefield redistribution.

In shallow subsurface layers, seismic attenuation has commonly been studied using spectral ratios, borehole and vertical seismic array recordings, coda-wave analysis, radiative-transfer modelling, and multiple lapse time window analysis (MLTWA) to separate intrinsic and scattering attenuation (Aki and Chouet, 1975; Fehler *et al.*, 1992; Hoshiba, 1993; Sato *et al.*, 2012). In buildings, attenuation is more often expressed through modal damping ratios estimated from ambient vibrations, earthquake records, random decrement techniques, frequency-domain decomposition, seismic interferometry, and system-identification methods (Tamura *et al.*, 2004; Snieder and Şafak, 2006; Bernal *et al.*, 2012; Cruz and Miranda, 2021). These studies show that building damping is important for structural response, but difficult to estimate reliably because it depends on vibration amplitude, structural period, soil–structure interaction, radiation damping, non-structural components, and identification uncertainty.

Despite this progress, the separation of apparent intrinsic and scattering attenuation within a coupled building–shallow-subsoil system remains limited. It is not yet well established how attenuation varies vertically from a building through the near surface into the underlying half-space, nor how robustly MLTWA can be applied at this small spatial scale. This study, therefore, addresses this gap using vertical-array recordings from a 16-story reinforced-concrete building and co-located boreholes. We adapt an MLTWA-based radiative-transfer approach to estimate frequency-dependent Q_i, Q_{sc}, and Q_s in three domains: the building, the shallow near-surface (depth of 0–50 m), and the underlying half-space (> 50 m).

2. Study area and dataset

2.1. Geology of the study area

The study site is in the Ataköy district of Istanbul, Turkey (Fig. 1). Beneath Ataköy, a thin alluvial cover overlies a thick Tertiary sequence (the Bakırköy and Güngören formations), underlain by Palaeozoic bedrock. The surface layer consists of unconsolidated alluvium (gravel, sand, silt, clay) (Sørensen *et al.*, 2006). The Bakırköy Formation is an off-white, porous lacustrine limestone with weak marl and interbedded green clay layers (Kurnaz *et al.*, 2011); the Güngören Formation comprises green, fissured, over-consolidated clays and clayey siltstones (Kurnaz *et al.*, 2011). The Palaeozoic basement (likely the Trakya Formation) includes interbedded sandstone, greywacke, and shale.

At the study site, the local stratigraphic sequence is constrained more directly by the available borehole logs and shear-wave velocity profile shown in Fig. 2. The borehole logs at the study site indicate light-brown, hard, gravelly sandy clay extending to approximately 15 m of depth, followed by a limestone-dominated interval between approximately 15 and 35 m. Clay interlayers occur near 35 m, while very dense sandy clay or clayey sand is observed from approximately 110 m to the deepest sensor depth of 140 m.

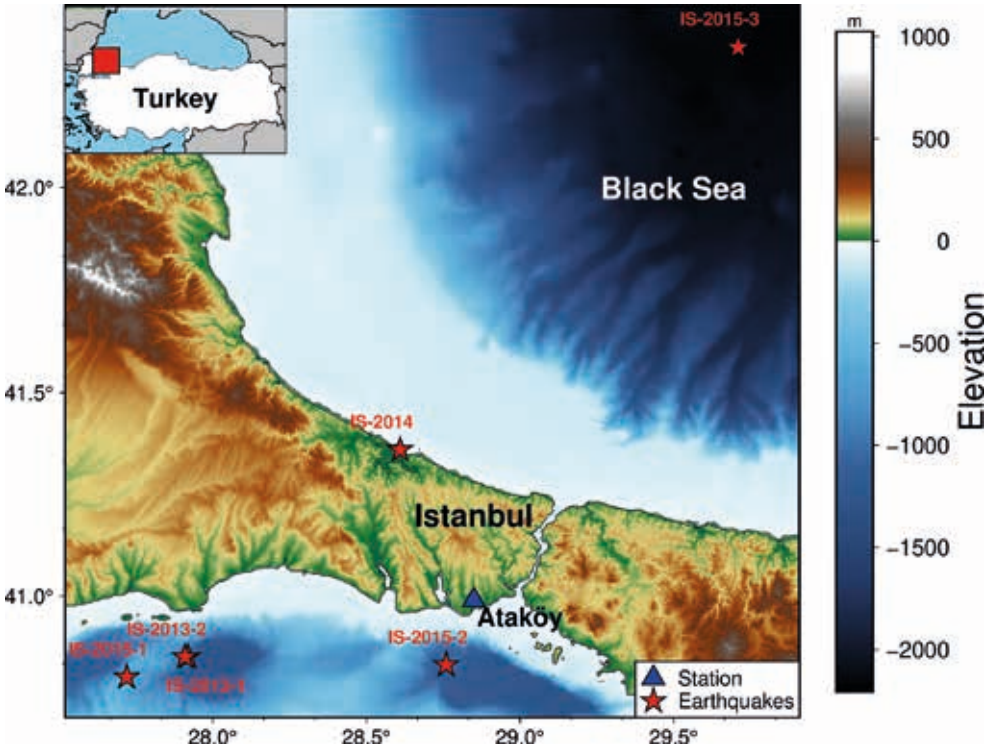


Fig. 1 - Map showing the Ataköy study site in Istanbul, Turkey (blue triangle) and the epicentres of the six earthquakes analysed in this study (red stars).

2.2. Description of the 'B22' building

The building measures 46.65 m tall from the foundation to the roof, including the basement but excluding the elevator machine room. Each floor has a standard height of 2.81 m, except for the basement, which is 4.0 m deep (Petrovic *et al.*, 2018a). The building has a foundation with dimensions of 23.1 m × 23.9 m. The exterior walls of the building, which feature windows, were constructed using precast panels. The interior and remaining exterior walls are made of reinforced concrete, with thicknesses of 15 cm and 20 cm, respectively.

2.3. Instrumentation and installation

Seismic data used in this study were acquired from a vertical array of accelerometers installed both within a building and the subsurface beneath it. A borehole accelerometer array was installed in December 2005 as part of a joint research project between the Kandilli Observatory and Earthquake Research Institute (KOERI) of Bogazici University in Istanbul, Turkey, and the German Research Centre for Geosciences (GFZ) (Parolai *et al.*, 2010).

Seismic sensors were installed at the surface (0 m) and within four boreholes extending to depths of 25, 50, 70, and 140 m. Ten years later, in September 2015, the B22 building was instrumented with a self-organising seismic early warning information network (SOSEWIN) (Picozzi *et al.*, 2009b) array consisting of 15 stations. Although the building was instrumented with 15 SOSEWIN stations distributed over seven floors, only the four stations equipped with Güralp 5TC accelerometers were used in the attenuation analyses because the micro-electro-

mechanical system recordings exhibited insufficient signal quality for the selected earthquakes. The four stations equipped with Güralp 5TC strong motion accelerometers were placed near the building's core and along the fire escape staircase on different floors (Fig. 2).

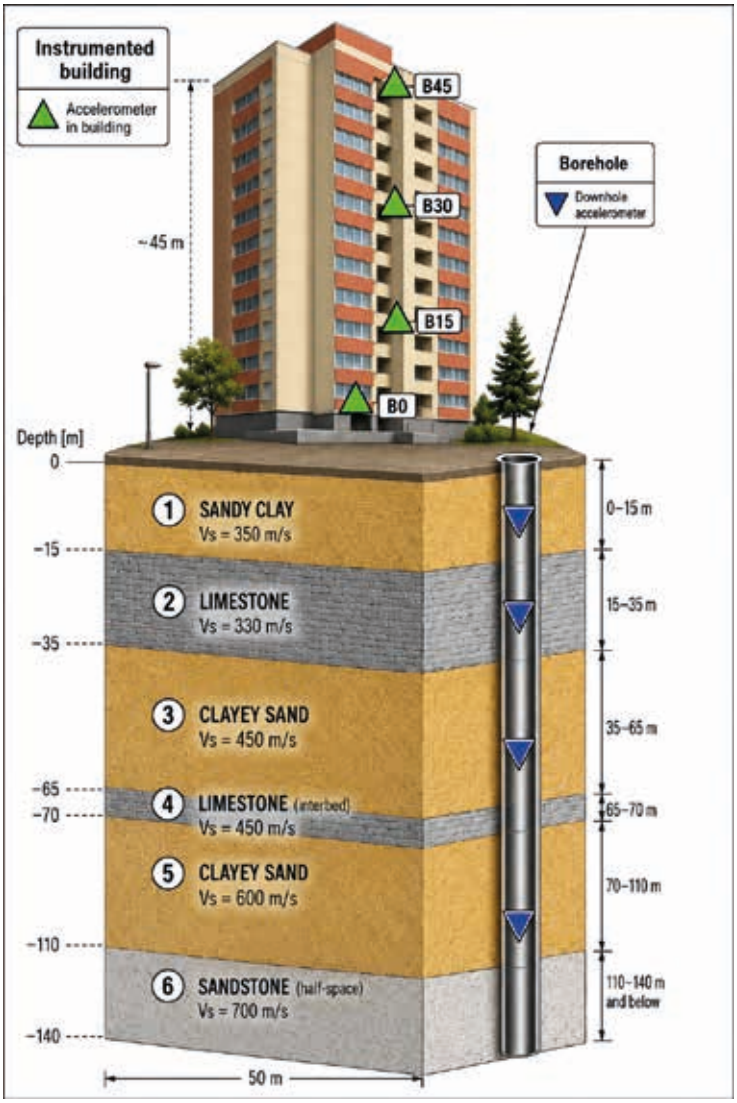


Fig. 2 - Instrumented B22 building and adjacent borehole array. Top: seismic sensors installed in the building at selected elevations. Subsurface: shear-wave velocity profile after Parolai *et al*. (2010), simplified stratigraphy, and borehole sensor depths. The building image is courtesy of the Bakırköy Courthouse, Republic of Turkey Ministry of Justice.

2.4. Earthquake datasets

This study uses a dataset comprising recordings from six earthquakes (Table 1), with moment magnitudes ranging from M_w 3.7 to 4.8 and epicentral distances from 20 to 165 km, occurring between November 2013 and December 2015. Four of these earthquakes were located in the Marmara Sea region (Fig. 1).

Events 4–6 were recorded after the expanded SOSEWIN (Picozzi *et al.*, 2009a) array was installed. Seismic data from the 70 m borehole sensor is unavailable for three events due to malfunctioning instruments. To fill this gap, the missing value was replaced by the mean seismic-

energy integral calculated from three earthquakes with complete recordings at a 70 m depth. To assess the influence of this substitution, the inversion was repeated after excluding the 70 m observation for the affected earthquake. The resulting parameter differences were less than 1%, indicating that the substitution had a negligible effect on the inversion results.

An example of the E–W component accelerograms recorded by the vertical array of sensors installed in the boreholes and on the building during the 2015 Istanbul earthquake is presented in Fig. 3.

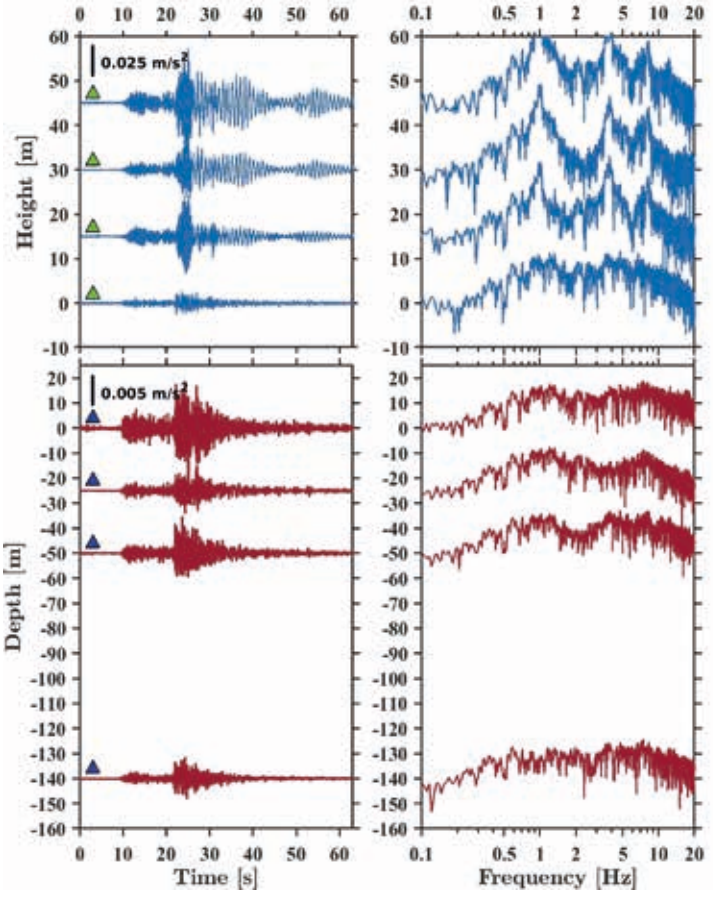


Fig. 3 - Example of E–W component accelerograms and corresponding Fourier amplitude spectra recorded by building (top panels) and borehole (bottom panels) sensors during the 2015 Istanbul earthquake. Traces are plotted by elevation (top) and depth (bottom), with triangles indicating sensor locations.

Table 1 - Summary of earthquake events recorded at the Ataköy study site in Istanbul, Turkey. The table lists the event identifier (ID), origin time, epicentral location, depth, moment magnitude (M_w), and epicentral distance from the Ataköy station (Petrovic *et al.*, 2018b).

Event ID	Date	Time (UTC)	Location	Depth (km)	Magnitude (M_w)	Distance (km)
IS-2013-1	27-Nov-2013	04:13:37	40.85° N, 27.92° E	9	4.8	80
IS-2013-2	27-Nov-2013	04:21:35	40.85° N, 27.91° E	7	4.0	80
IS-2014-1	05-Feb-2014	01:56:44	41.36° N, 28.61° E	2	3.7	45
IS-2015-1	28-Oct-2015	16:20:03	40.80° N, 27.72° E	6	4.6	100
IS-2015-2	16-Nov-2015	15:45:43	40.83° N, 28.76° E	8	4.3	20
IS-2015-3	15-Dec-2015	01:13:39	42.34° N, 29.71° E	0	4.1	165

2.5. Data preprocessing

Raw accelerograms were de-trended, tapered, and band-pass filtered between 0.1 and 60 Hz (zero-phase). Velocity seismograms were, then, obtained by single integration of the preprocessed accelerations for the following step of computing energy integral. For each sensor, frequency band, and lapse-time window, the energy was obtained by integrating the squared three-component velocity amplitude. The detailed definition of the lapse-time windows used for the MLTWA analysis is given in Section 3.2.

3. Methodology

3.1. Theoretical background of MLTWA

MLTWA is a widely used method for estimating intrinsic and scattering attenuation from the temporal evolution of seismic wave energy (Hoshiba, 1991, 1997; Fehler *et al.*, 1992). The method is based on the radiative transfer theory which describes the propagation of seismic energy in heterogeneous media as a combination of energy loss due to intrinsic absorption and energy redistribution caused by scattering. Intrinsic attenuation converts seismic energy into heat, resulting in an irreversible loss of energy, whereas scattering attenuation redistributes energy through interactions with heterogeneities without necessarily removing energy from the wavefield.

Operationally, MLTWA analyses the seismic energy recorded after the S-wave arrival in several consecutive lapse-time windows. Early S-wave windows are dominated by direct and weakly scattered waves, while successive windows contain progressively larger contributions from multiply scattered energy. Because intrinsic attenuation and scattering attenuation affect the temporal evolution of seismic energy differently, the observed energy integrals between successive lapse-time windows can be compared with radiative-transfer predictions to estimate the corresponding attenuation parameters (Fehler *et al.*, 1992; Hoshiba, 1997).

To estimate the attenuation parameters responsible for the observed energy distribution, the measured normalised energy integrals were compared with theoretical predictions based on radiative-transfer theory. For an isotropic, homogeneous medium, the analytical solutions of Zeng *et al.* (1991) and Paasschens (1997) were used, whereas the numerical formulation of Hoshiba (1997) was used for layered or depth-dependent media. These models predict the spatial and temporal distribution of seismic energy for specified intrinsic and scattering attenuation coefficients.

In the radiative-transfer framework, attenuation is described by two frequency-dependent coefficients: the scattering *g(f)* and the intrinsic *h(f)* attenuation coefficients, both expressed in km^{-1}. The inverse extinction length and seismic albedo were also calculated from the retrieved attenuation coefficients. The inverse extinction length is defined as $Le^{-1}(f) = g(f) + h(f)$, where $Le^{-1}(f)$ has units of km^{-1}. The corresponding extinction length is $Le = \frac{1}{g(f)+h(f)}$ and represents the characteristic propagation distance over which seismic-wave energy is reduced by the combined effects of scattering and intrinsic absorption. Seismic albedo is defined as $B_0(f) = \frac{g(f)}{g(f)+h(f)}$. It is dimensionless and describes the relative contribution of scattering to total attenuation. Values of B_0 close to 1 indicate that scattering dominates, whereas values close to 0 indicate that intrinsic absorption dominates.

For an S-wave velocity V_s expressed in km s^{-1} and angular frequency $\omega = 2\pi f$, the scattering, intrinsic, and total quality factors are defined as

$$Q_{sc}(f) = \frac{\omega}{g(f)V_s} \quad (1)$$

$$Q_i(f) = \frac{\omega}{h(f)V_s} \quad (2)$$

and

$$Qs(f) = \frac{\omega}{[h(f) + g(f)]V_s} \quad (3)$$

respectively. V_s values used to convert the attenuation coefficients into quality factors are specified in Section 4, together with the separate building model and the two-layer subsoil model.

3.2. Application to vertical array of seismograms

The MLTWA concept was applied to evaluate the lapse-time distribution of seismic energy along the vertical building–borehole array. Classical MLTWA estimates intrinsic and scattering attenuation from the temporal decay and redistribution of seismic energy in successive lapse-time windows. In this study, the same lapse-time energy principle was adapted to a compact vertical seismic array. The regional S-coda generated by regional earthquakes is interpreted as an already-developed wavefield arriving at the site, and the vertical seismic array samples how this energy is locally modified with elevation in the building and deep in the borehole.

For each event, sensor, and frequency band, the S-wave arrival time t_s was first picked. Three consecutive 15 s lapse-time windows were then defined relative to t_s: W_1 from 0 to 15 s, W_2 from 15 to 30 s, and W_3 from 30 to 45 s after the S-wave arrival. The first window contains the direct S-wave and early scattered energy, whereas the second and third windows contain progressively later coda energy. Fig. 4 illustrates the window selection on a representative seismogram.

Coda normalisation was, then, applied independently at each sensor depth or elevation. A late reference coda window was selected from 55–65 s after t_s, corresponding to a 10 s window centred at 60 s after the S-wave arrival. For each sensor and frequency band, the energies in W_1, W_2, and W_3 were divided by the energy in the corresponding reference window at the same sensor. Thus, normalisation does not use a common reference station or depth; instead, it is performed locally for each sensor. This procedure reduces the effects of source amplitude, instrument gain, and site amplification, and emphasises the relative redistribution of energy among the lapse-time windows across the vertical array.

Because the hypocentral distances of the analysed earthquakes are much greater than the vertical aperture of the building–borehole array, the incident wavefield was approximated as locally planar over the scale of the array. Event-specific hypocentral distances were considered for the source-to-site propagation. However, no additional depth-dependent spherical-spreading correction was applied between individual sensors, since the maximum vertical sensor separation is negligible relative to earthquake distances.

Because IS-2015-2 is the nearest event in the dataset, at approximately 20 km, its influence on the attenuation estimates was tested separately. A leave-one-event-out inversion was performed by excluding IS-2015-2. The resulting changes in Q_s were +8.3% at 3 Hz, −7.9% at 5 Hz, −9.0% at 6 Hz, and −9.0% at 10 Hz. These changes are small, indicating that the final attenuation estimates are not strongly controlled by this nearest event. Therefore, IS-2015-2 was retained in the multi-event inversion, although its late-window coda contribution was interpreted cautiously.

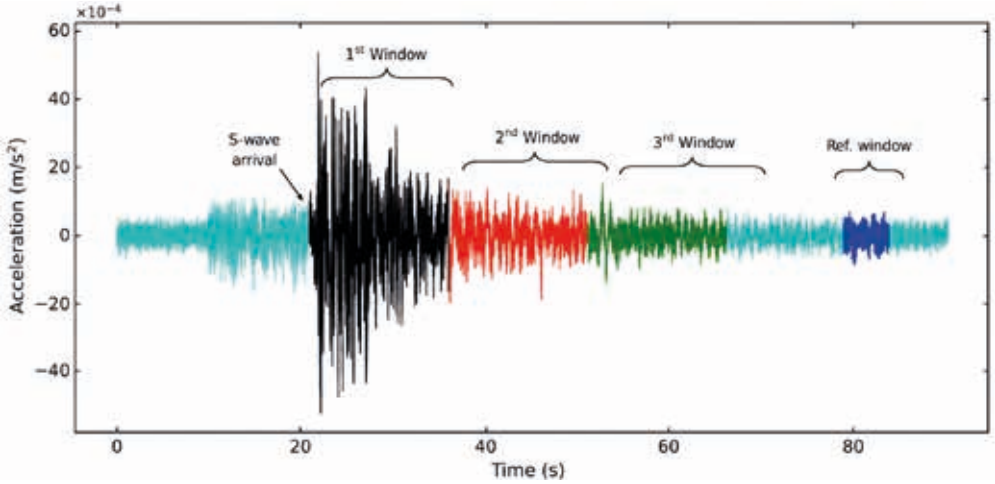


Fig. 4 - Example seismogram windows used for MLTWA. The waveform is divided into three consecutive lapse-time windows, W_1, W_2, and W_3, following the S-wave arrival and a reference coda window centred around 60 s after the S-wave arrival.

For each frequency band, the normalised windowed energy integrals were compared along the vertical profile and fitted using three-dimensional (3D) radiative-transfer solutions within a simplified building–subsoil model. This approach evaluated the local modification of incoming coda energy with building elevation and borehole depth. The observed vertical variations in lapse-time energy were interpreted mainly in terms of intrinsic absorption, scattering-related energy redistribution, impedance contrasts, near-surface reverberation, and soil–structure interaction. Because the array aperture was much smaller than that used in classical MLTWA applications, the retrieved attenuation parameters were interpreted as effective attenuation values rather than fully resolved intrinsic and scattering properties of a large homogeneous medium.

3.3. Inversion approach

3.3.1. Misfit function

Theoretical energy integrals were calculated using the analytical solution of Paasschens (1997) for the homogeneous model and the numerical solution of Hoshiba (1997) for the layered model. The inversion sought the pair of parameters (g, h) that minimised the difference between the observed and theoretical normalised energy integrals, where g and h are the scattering and intrinsic attenuation coefficients, respectively.

The misfit function measured the logarithmic difference between the observed and theoretical energy integrals and was defined as:

$$E(g,h) = \sum_{k=1}^{N}\sum_{i=1}^{3}\left\{log_{10}\left[EI_{obs(i)}(r_k)\right] - log_{10}\left[EI_{theor(i)}(g,h,r_k)\right]\right\}^2 \quad (4)$$

where $EI_{obs,i}$ and $EI_{theor,i}$ denote the observed and theoretical energy integrals for lapse-time window i, respectively; i = 1, 2, 3 indexes the three lapse-time windows; k indexes the observations; N is the total number of observations; and r_k is the propagation distance associated with observation

k. The logarithmic formulation reduced the influence of differences in amplitude scale and large outliers, while the three lapse-time windows preserved information on the temporal evolution of the coda energy. The misfit was minimised using a hybrid procedure combining grid search and simulated annealing.

3.3.2. Hybrid inversion using grid search and simulated annealing

A two-stage inversion combining a coarse grid search and simulated annealing was used to fit the observed normalised energy integrals with radiative-transfer predictions.

Stage 1: coarse grid search. An exploratory grid search was first performed over broad ranges of the scattering and intrinsic attenuation coefficients. For the building, which was inverted separately as a single domain, 2,500 combinations of g_b and h_b were tested. The scattering coefficient ranged from 0.03 to 1.50 km^{-1} in increments of 0.03 km^{-1}, whereas the intrinsic attenuation coefficient ranged from 0.01 to 0.50 km^{-1} in increments of 0.01 km^{-1}. The grid search identified the region of lowest misfit in the (g_b, h_b) parameter space and provided an initial model for simulated-annealing refinement.

The subsoil was represented by a two-layer model in which the shallow-layer coefficients g_1 and h_1 and half-space coefficients g_2 and h_2 were estimated simultaneously. Because an exhaustive four-parameter grid search would require a prohibitively large number of forward simulations, the coarse search was used only to identify suitable initial parameter ranges.

Stage 2: simulated annealing refinement. Simulated annealing (Kirkpatrick *et al.*, 1983) was, then, used to optimise g_b and h_b for the building and g_1, h_1, g_2, and h_2 for the subsoil. Candidate models were generated by randomly perturbing the model parameters. A quadratic cooling schedule was adopted:

$$T_k = 0.2E_0\left(\frac{N_{iter} - k + 1}{N_{iter}}\right)^2, \tag{5}$$

where E_0 is the initial misfit, k is the iteration number, and N_{iter} is the maximum number of iterations. For N_{iter} = 100, the temperature decreased from 2.0 E_0 to $2 \times 10^{-5} E_0$. Models with lower misfit were accepted automatically, whereas higher-misfit models were accepted according to the Metropolis probability:

$$P = exp\left[\frac{-(E_{new} - E_{old})}{T_k}\right].$$

Convergence was evaluated from the stabilisation of the misfit and the accepted g and h values during the final iterations, together with their consistency with the grid-search minimum. Each iteration required a complete radiative-transfer simulation. The inversion was, therefore, terminated after 100 iterations or earlier when the misfit decreased below the target misfit $E(g,h)$ = 0.01. Fig. 5 illustrates simulated-annealing convergence at f = 11 Hz, including misfit evolution, the intrinsic attenuation coefficient h updates, and the temperature (cooling) schedule. The retrieved coefficients were subsequently converted into intrinsic, scattering, and total quality factors.

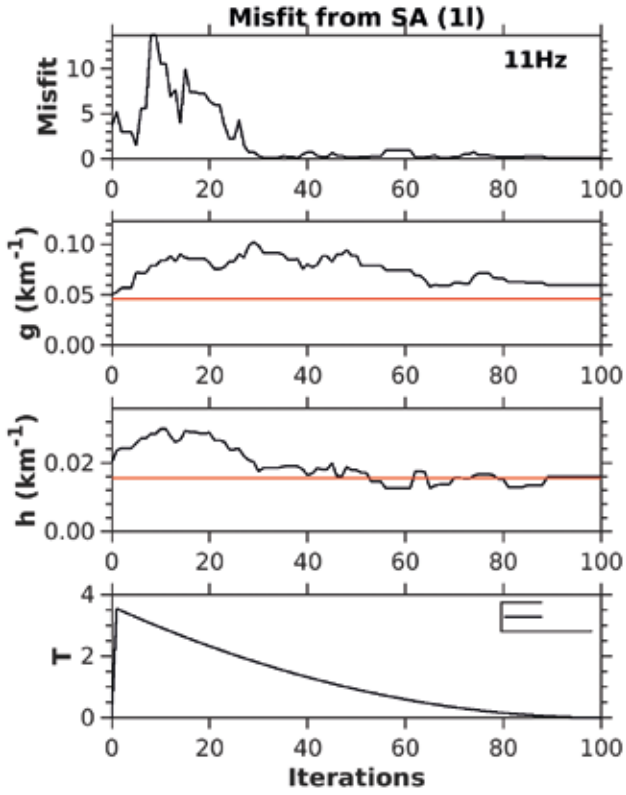


Fig. 5 - Example of the simulated-annealing inversion at 11 Hz. Top: evolution of the misfit. Middle: accepted scattering coefficient *g* and intrinsic attenuation coefficient *h*, expressed in km^{-1}, as functions of the iteration numbers. Bottom: temperature T_k associated with the quadratic cooling schedule.

3.4. Methodological limitations

Classical MLTWA assumptions, including isotropic multiple scattering in a statistically homogeneous 3D medium, are not strictly satisfied at the scale of the building–subsoil array. The retrieved parameters are, therefore, interpreted as apparent effective attenuation values that may include material damping, scattering, reverberation, radiation damping, and wavefield complexity. The implications of these limitations are discussed in Section 5.4.

4. Results

4.1. Modelling assumptions and parametrisation

The attenuation inversion was performed using a simplified building–soil model composed of the 46 m high B22 building overlying a two-zone subsoil representation (Fig. 6). The subsoil was divided into an upper 0–50 m zone and a deeper half-space.

The 50 m boundary was introduced as a practical discretisation depth for the inversion, rather than as a sharp lithological or velocity interface. This parametrisation separates the upper part of the borehole array, which samples the shallow near-surface deposits, from the deeper sensors used to represent the underlying formation. The upper and lower zones are, therefore, interpreted as effective attenuation regions rather than as detailed geological layers.

Layer-averaged shear-wave velocities of 0.39 km/s and 0.65 km/s were used to convert the attenuation coefficients into quality factors for the upper and lower subsoil zones, respectively.

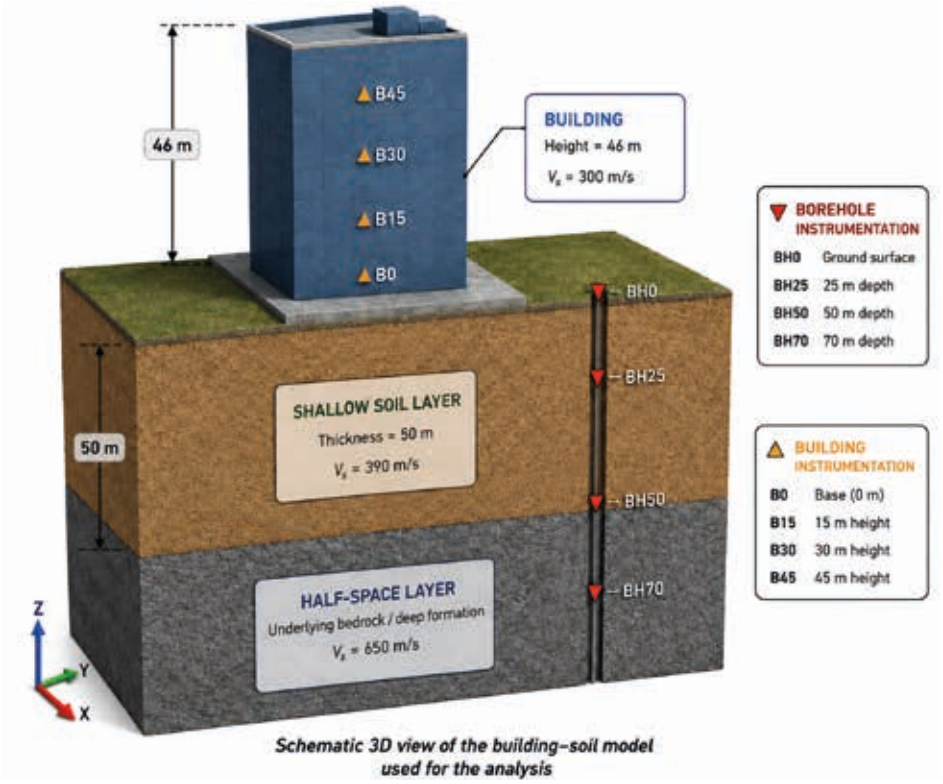


Fig. 6 - Schematic building–subsurface model used for the attenuation analysis: a homogeneous 46-m-high building overlying an effective two-zone subsoil representation composed of an upper 0–50 m zone and a deeper half-space.

An effective shear-wave velocity of approximately 0.30 km/s was assumed for the B22 building, consistent with previous deconvolution-based analyses of the same structure (Petrovic *et al.*, 2018a).

Although the borehole log and shear-wave velocity profile indicate gradual and local variations with depth, the available sensor spacing and the relatively short propagation distances within the building–subsoil system do not provide sufficient resolution to independently constrain attenuation parameters for each individual geological unit. A more detailed multi-layer model would introduce additional scattering and intrinsic attenuation parameters, increasing the non-uniqueness of the inversion and the risk of over parametrisation.

To describe the frequency dependence consistently across the three domains, the estimated intrinsic, scattering, and total quality factors were fitted using the power-law relation $Q(f) = Q_0 f^n$, where Q_0 is the quality factor at 1 Hz and n is the frequency-dependence exponent. Attenuation parameters were estimated over the 1–16 Hz frequency range. The power-law fits were calculated over 1–16 Hz for the building and underlying half-space, and over 3–16 Hz for the shallow 0–50 m layer, where the estimates exhibited a stable log–log trend. The domain-specific relationships and uncertainty bounds are presented in Sections 4.2 to 4.4 and summarised in Table 2.

4.2. Attenuation estimates in the reinforced concrete building (B22)

For the B22 building, the best-fitting relationships were $Q_{sc}(f) = 6.05f^{1.14}$, $Q_i(f) = 22f^{1.03}$, and $Q_s(f) = 4.78f^{1.14}$. Fig. 7 shows the corresponding inverse quality factors and power-law fits.

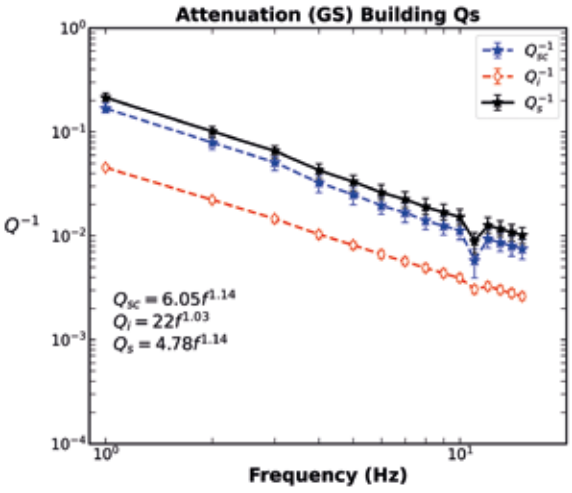


Fig. 7 - Inversion-derived attenuation parameters for the B22 building. The curves show the inverse total, intrinsic, and scattering quality factors, Q_s^{-1}, Q_i^{-1}, and Q_{sc}^{-1}, respectively, together with the corresponding power-law fits over the 1–16 Hz frequency range. Error bars indicate uncertainty bounds derived from the 10% low-misfit region of the *g*–*h* misfit surface.

4.3. Attenuation estimates near surface (depth 0–50 m)

For the shallow 0–50 m layer, the best-fitting relationships were $Q_{sc}(f) = 4.05f^{1.63}$, $Q_i(f) = 2.82f^{1.73}$, and $Q_s(f) = 1.64f^{1.69}$. Fig. 8a shows the corresponding inverse quality factors, whereas Fig. 8b compares the observed and predicted normalised energy integrals at 11 Hz.

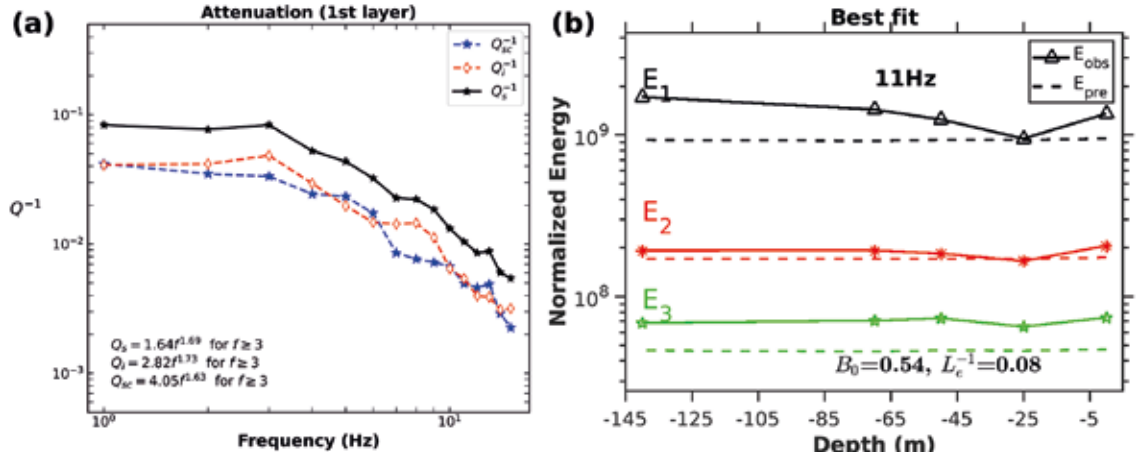


Fig. 8 - Attenuation results for the shallow near-surface layer (0–50 m): a) frequency dependence of the estimated intrinsic, scattering, and total attenuation parameters; b) comparison between observed (E_{obs}) and predicted (E_{pre}) normalised energy integrals at 11 Hz for the best-fitting model.

4.4. Attenuation estimates in half-space domain (depth > 50 m)

For the underlying half-space, the best-fitting empirical relationships were $Q_{sc}(f) = 41f^{1.00}$, $Q_i(f) = 47.5f^{0.92}$, and $Q_s(f) = 22f^{0.96}$. Fig. 9a shows the corresponding inverse quality factors, whereas Fig. 9b compares the observed and predicted normalised energy integrals at 15 Hz.

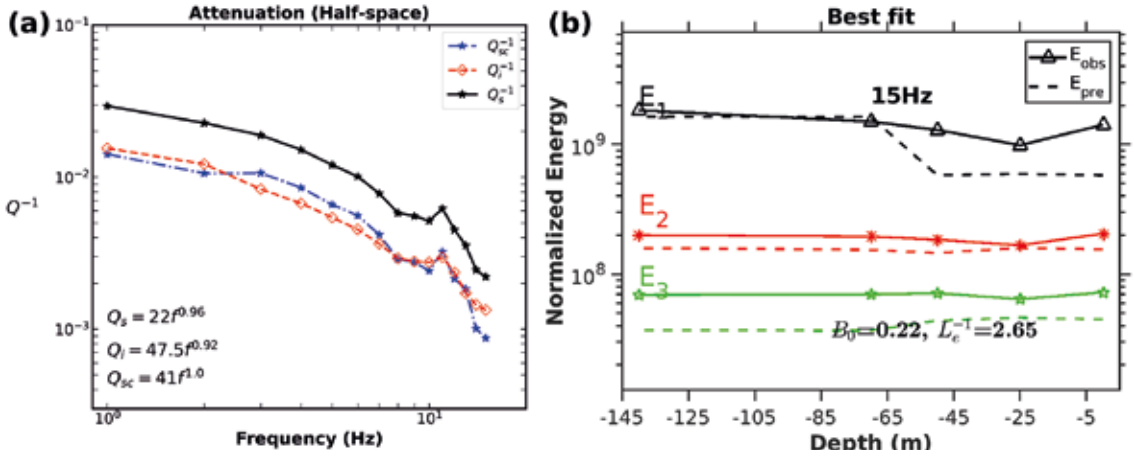


Fig. 9 - Attenuation results for the underlying half-space at depths greater than 50 m: a) frequency dependence of the estimated intrinsic, scattering, and total attenuation parameters; b) comparison between observed (E_{obs}) and predicted (E_{pre}) normalised energy integrals at 15 Hz for the best-fitting model.

4.5. Validation and comparison with alternative methods

To validate the attenuation values obtained from the MLTWA on building B22, we applied two independent approaches based on the building's fundamental-mode response. First, the fundamental-mode damping ratio was estimated from five roof accelerograms using the logarithmic decrement method. The mean damping ratio is ζ = 1.98%, corresponding to $Q = \frac{1}{(2\zeta)}$ = 25.3. A complementary estimate using the half-power bandwidth of the resonance peak gives Q = 27. The agreement supports the order of magnitude of the apparent intrinsic attenuation estimated near the building's fundamental frequency, although it does not independently validate the separation of intrinsic and scattering contributions.

In addition, the normal-mode oscillation method of Snieder and Şafak (2006) and Newton and Snieder (2012) was applied using deconvolution interferometry. The basement recording was used as the reference signal to calculate impulse-response functions for each floor. Fig. 10a

Table 2 - Best-fitting frequency-dependent attenuation relationships and uncertainty bounds for the B22 building, shallow near-surface layer, and underlying half-space. Uncertainty bounds were derived from the 10% low-misfit region of the g – h misfit surface. Reference quality-factor values at 5 and 10 Hz were calculated from the corresponding best-fitting relationships.

Domain	Parameter	Best-fitting relation	Uncertainty range	Q (5 Hz)	Q (10 Hz)
Building (B22)	$Q_i(f)$	$22f^{1.03}$	$[20.74f^{1.06}, 23.28f^{1.08}]$	115	236
Building (B22)	$Q_{sc}(f)$	$6.05f^{1.14}$	$[6.0f^{1.14}, 6.47f^{1.26}]$	38	84
Building (B22)	$Q_s(f)$	$4.78f^{1.14}$	$[4.14f^{1.14}, 5.07f^{1.21}]$	30	66
Shallow near-surface layer, 0–50 m	$Q_i(f)$	$2.82f^{1.73}$	$[1.66f^{1.48}, 4.78f^{1.98}]$	46	151
Shallow near-surface layer, 0–50 m	$Q_{sc}(f)$	$4.05f^{1.63}$	$[2.38f^{1.38}, 6.9f^{1.87}]$	56	173
Shallow near-surface layer, 0–50 m	$Q_s(f)$	$1.64f^{1.69}$	$[1.16f^{1.52}, 2.35f^{1.85}]$	25	80
Half-space, > 50 m	$Q_i(f)$	$47.5f^{0.92}$	$[39f^{0.95}, 57.7f^{0.89}]$	209	395
Half-space, > 50 m	Qsc (f)	$41.0f$ 1.0	$[27.8f^{1.07}, 60f^{0.93}]$	205	410
Half-space, > 50 m	Qs (f)	$22.0f$ 0.96	$[16.7f^{1.01}, 29.5f^{0.91}]$	103	201

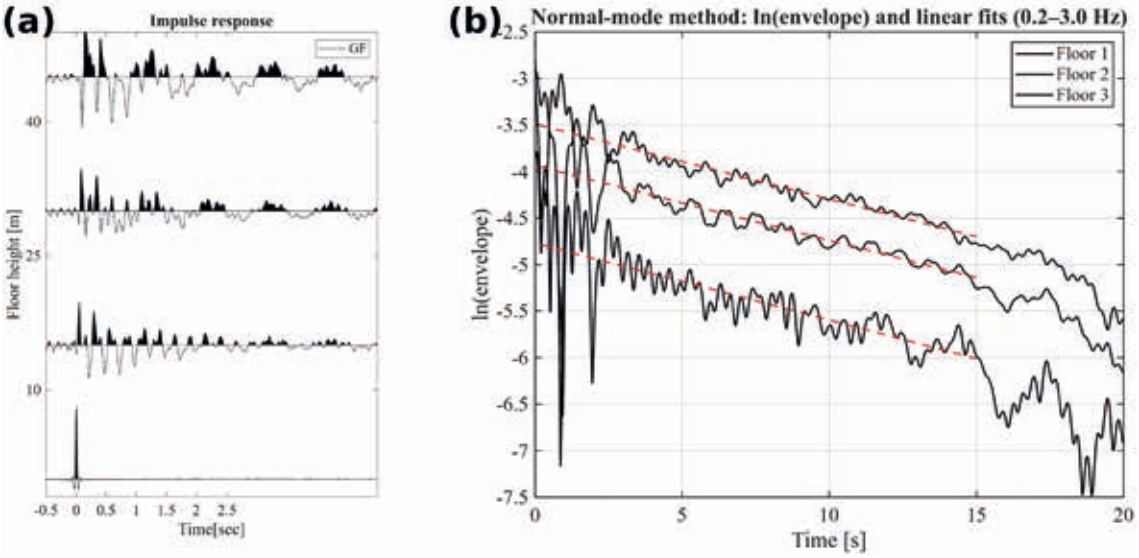


Fig. 10 - a) Impulse-response functions of the B22 building obtained by deconvolving the motions recorded at successive floors with respect to the basement recordings. b) Natural logarithms of the corresponding signal envelopes, with dashed lines indicating the least-squares linear fits.

shows the deconvolved waveforms band-pass filtered between 0.2 and 3.0 Hz. The basement response appears as a narrow, band-limited pulse at $t = 0$, whereas the responses at $t > 0$ represent the building's reaction to an impulsive excitation dominated by the fundamental mode, with a period of approximately 0.98 s. The amplitude and duration of the responses increase towards the upper floors, reflecting structural resonance and energy-trapping effects. The impulse-response functions were band-pass filtered between 0.2 and 3.0 Hz, and the natural logarithm of each signal envelope was fitted with a linear function. Fig. 10b shows the logarithmic envelopes together with the corresponding least-squares linear fits. The negative slope of each fit represents the exponential decay rate of the modal response and was used to estimate the associated damping or quality factor.

5. Discussion

5.1. Physical interpretation of the estimated quality factors in the building

Wave propagation within the building is interpreted as a predominantly one-dimensional (1D) reverberation process controlled by roof–base reflections, floor-to-floor impedance contrasts, structural heterogeneity, and radiative energy leakage into the soil. The echo peaks in the roof-accelerogram autocorrelation (Fig. 11) indicate repeated vertical reflections, whose decay reflects material damping, interface-related energy redistribution, and radiation damping.

The regional S-wave coda arriving at the building base is subsequently modified by structural resonance and reverberation. Because inter-storey transmission remains largely coherent within the approximately vertical waveguide geometry, strong internal multiple scattering is unlikely, consistent with the deconvolution results.

The intrinsic-quality-factor relation obtained from MLTWA, $Q_i(f) = 22f^{1.03}$, is physically plausible. At 1 Hz, $Q_i(1) = 22$, which is close to the modal-quality-factor estimate derived from the measured

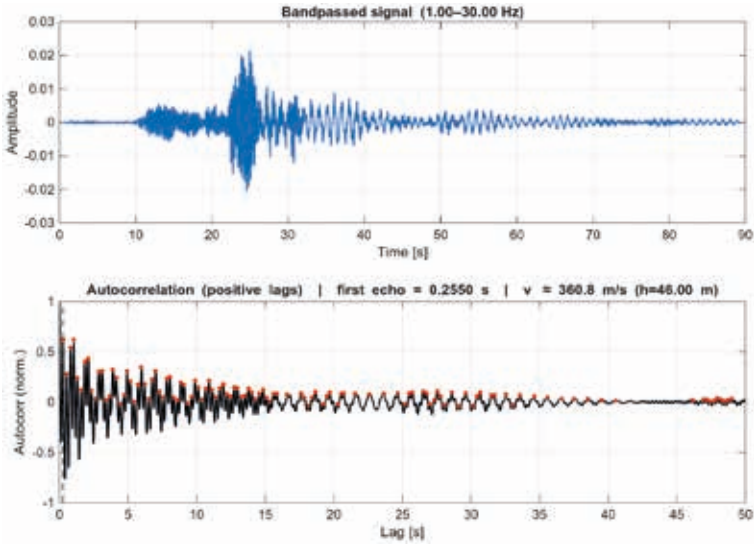


Fig. 11 - Roof accelerogram and corresponding autocorrelation used to identify repeated vertical reflections in the B22 building. The accelerogram was band-pass filtered between 1 and 30 Hz and the autocorrelation was normalised by its maximum amplitude. The first prominent echo occurs at approximately $\Delta t_{echo} = 2\,\frac{H}{V_s} \approx 0.255$ s.

damping ratio at the fundamental mode. For $\zeta = 1.98\%$, the lightly damped approximation gives $Q = \frac{1}{2\zeta} \approx 25.3$. This agreement supports the interpretation that material damping contributes substantially to the observed energy loss. However, the modal estimate represents the combined damping of the structural system and cannot be interpreted as an independent measurement of intrinsic attenuation alone. In addition, structural reverberation may be mapped onto an apparently large scattering coefficient, g, leading to an underestimated Q_{sc}, while radiation damping may contribute to the apparent intrinsic attenuation coefficient h. The building values of Q_i, Q_{sc}, and Q_s are, therefore, interpreted as effective attenuation parameters rather than as uniquely separated physical mechanisms.

5.2. Physical interpretation of estimated quality factors in near surface and half-space media

Anelastic absorption and wavefield redistribution caused by small-scale heterogeneity strongly influence attenuation in the shallow near-surface layer. Both $Q_{sc}(f) = 4.05f^{1.63}$ and $Q_i(f) = 2.82f^{1.73}$ rapidly increase with frequency, indicating that scattering and intrinsic attenuation become weaker at higher frequencies. Because Q_i is consistently lower than Q_{sc}, intrinsic absorption is stronger than scattering attenuation throughout the analysed frequency range. The low Q_i and Q_{sc} values at low frequencies indicate strong energy loss, consistent with the unconsolidated and heterogeneous materials of the shallow subsurface.

In the half-space below 50 m, $Q_{sc}(f) = 41f^{1.00}$ and $Q_i(f) = 47.5f^{0.92}$ have similar magnitudes and frequency dependences, indicating that scattering and intrinsic dissipation contribute comparably to the total attenuation. Both quality factors increase approximately linearly with frequency. Similarly, $Q_s(f) = 22f^{0.96}$ increases almost linearly, indicating that total attenuation decreases with increasing frequency. Overall, intrinsic absorption dominates in the shallow 0–50 m layer, whereas intrinsic and scattering attenuation are of comparable magnitude in the underlying half-space. The decrease in scattering attenuation with depth is consistent with reduced small-scale heterogeneity and agrees with previous MLTWA studies (Hoshiba, 1997; Hoshiba *et al.*, 2001; Giampiccolo *et al.*, 2006).

5.3. Comparison with previous work

Regional MLTWA studies have shown that the relative contributions of intrinsic and scattering attenuation vary substantially with geological setting, frequency, and propagation path. Fehler *et al.* (1992) separated intrinsic and scattering attenuation in the Kanto–Tokai region of Japan, whereas Hoshiba *et al.* (2001), Giampiccolo *et al.* (2006), and Del Pezzo *et al.* (2011) demonstrated that Q_i, Q_{sc}, seismic albedo, and extinction length can vary with depth and regional heterogeneity. These findings support the interpretation that the attenuation parameters estimated in this study represent site- and depth-dependent effective values.

At 5 Hz, the estimated values are 25 for the shallow 0–50 m layer and 103 for the underlying half-space. These values are comparable to the averages of 30, 46, and 99 reported by Parolai *et al.* (2010) for depth intervals extending to 50, 70, and 140 m, respectively, and to the near-surface range of 10–100 m reported by Hutchings and Viegas (2012). The agreement supports the overall magnitude and depth dependence of the estimated attenuation, although the relative intrinsic and scattering contributions differ between the two domains.

5.4. Limitations of applying MLTWA to buildings

Buildings behave predominantly as quasi-1D vertical waveguides rather than the isotropic 3D scattering media assumed by classical MLTWA. Consequently, resonance and geometrical reverberation may be attributed to the scattering term, producing an overestimated apparent scattering coefficient and underestimated Q_{sc}. Radiation of vibrational energy into the soil and adjacent structural elements may likewise contribute to the apparent intrinsic attenuation. The building parameters should, therefore, be interpreted as effective values representing combined material damping, reverberation, scattering-related redistribution, and radiation damping.

5.5. Sensitivity and resolution of attenuation parameters

The misfit surface in Fig. 12 shows a narrow, diagonally oriented low-misfit valley in the *g–h* parameter space, indicating a slight trade-off between scattering and intrinsic attenuation. The best-fit model lies near the valley centre, but nearby combinations of *g* and *h* provide similar fits. This trade-off indicates that intrinsic attenuation is better resolved than scattering attenuation at this frequency, while *g* remains less constrained.

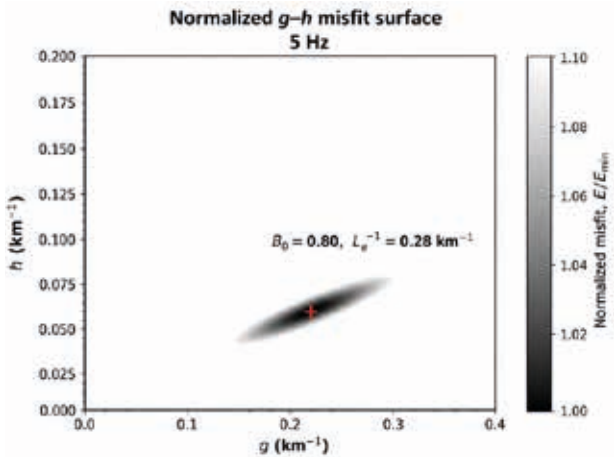


Fig. 12 - Two-dimensional misfit surface for 5 Hz using a one-layer velocity model. The red cross indicates the best-fit solution.

6. Conclusions

Attenuation was estimated in three domains: the B22 building, the shallow subsurface at depths of 0–50 m, and the underlying half-space below 50 m. The results show clear depth- and frequency-dependent variations. Attenuation is strongest in the shallow subsurface and decreases with depth, while both intrinsic and scattering quality factors generally increase with frequency.

The relative contributions of intrinsic and scattering attenuation differ among the three domains. In the building, $Q_{sc} < Q_i$ indicates a larger apparent scattering-related contribution; however, Q_{sc} may also reflect structural reverberation, resonance, and waveguide-like propagation. In the shallow 0–50 m layer, $Q_i < Q_{sc}$ indicates that intrinsic absorption dominates, whereas intrinsic and scattering attenuation are comparable in the underlying half-space.

Overall, the building modifies the incoming seismic energy through resonance, frequency-dependent redistribution, and soil–structure interaction. Because classical MLTWA assumes isotropic 3D media, the building attenuation parameters should be interpreted as apparent effective values rather than uniquely separated intrinsic and scattering properties. Nevertheless, the depth dependent attenuation pattern obtained in this study is consistent with the stronger attenuation observed in the shallow subsurface and the progressively weaker attenuation at greater depth. Future studies should incorporate anisotropic scattering, radiation damping, and waveguide-aware forward models to better separate attenuation mechanisms in building–soil systems.

Acknowledgments. This research was carried out as part of a doctoral project at the University of Trieste, Italy. Financial support was provided by the ICTP Training and Research in Italian Laboratories (TRIL) fellowship programme, with institutional support from the National Institute of Oceanography and Applied Geophysics – OGS. The author thanks colleagues at the OGS's Centre for Seismological Research (CRS) for their technical assistance. Preliminary results were presented at the 41st GNGTS Congress, Bologna, 7–9 February 2023. The data were collected as part of the CEDIM project 'Megacity: Istanbul,' in a collaboration between the Kandilli Observatory and Earthquake Research Institute (KOERI) of Boğaziçi University, Istanbul, Turkey, and the German Research Centre for Geosciences (GFZ), and were kindly made available by the latter.

REFERENCES

Aki K. and Chouet B.; 1975: *Origin of coda waves: source, attenuation, and scattering effects*. J. Geophys. Res., 80, 3322-3342, doi: 10.1029/JB080i023p03322.

Akinci A., Munafò I. and Malagnini L.; 2022: *S-wave attenuation variation and its impact on ground motion amplitudes during 2016–2017 Central Italy earthquake sequence.* Front. Earth Sci., 10, 903955, doi: 10.3389/feart.2022.903955.

Bernal D., Mozaffari Kojidi S., Kwan K. and Döhler M.; 2012: *Damping identification in buildings from earthquake records*. In: Huang M. (ed), Proceedings SMIP 2012 Seminar on Utilization of Strong-Motion Data, California Geological Survey, Sacramento, California, USA, pp. 39-56.

Cruz C. and Miranda E.; 2021: *Insights into damping ratios in buildings.* Earthq. Eng. Struct. Dyn., 50, 916–934, doi: 10.1002/eqe.3356.

Del Pezzo E., Bianco F., Marzorati S., Augliera P., D'Alema E. and Massa M.; 2011: *Depth-dependent intrinsic and scattering seismic attenuation in north central Italy.* Geophys. J. Int., 186, 373-381, doi: 10.1111/j.1365-246X.2011.05053.x.

Fehler M., Hoshiba M., Sato H. and Obara K.; 1992: *Separation of scattering and intrinsic attenuation for the Kanto-Tokai region, Japan, using measurements of S-wave energy versus hypocentral distance.* Geophys. J. Int., 108, 787-800, doi: 10.1111/j.1365-246X.1992.tb03470.x.

Giampiccolo E., Tuvè T., Gresta S. and Patanè D.; 2006: *S-waves attenuation and separation of scattering and intrinsic absorption of seismic energy in southeastern Sicily (Italy).* Geophys. J. Int., 165, 211-222, doi: 10.1111/j.1365-246X.2006.02881.x.

Hoshiba M.; 1991: *Simulation of multiple-scattered coda wave excitation based on the energy conservation law.* Phys. Earth Planet. Inter., 67, 123-136.

Hoshiba M.; 1993: *Separation of scattering attenuation and intrinsic absorption in Japan using the multiple lapse time window analysis of full seismogram envelope.* J. Geophys. Res., 98, 15809-15824, doi: 10.1029/93JB00347.

Hoshiba M.; 1997: *Seismic coda wave envelope in depth dependent S wave velocity structure.* Phys. Earth Planet. Inter., 104, 15-22.

Hoshiba M., Rietbrock A., Scherbaum F., Nakahara H. and Haberland C.; 2001: *Scattering attenuation and intrinsic absorption using uniform and depth-dependent model – application to full seismogram envelope recorded in Northern Chile*. J. Seismol., 5, 157-179, doi: 10.1023/A:1011478202750.

Hutchings L. and Viegas G.; 2012: *Application of empirical Green's functions in earthquake source, wave propagation and strong ground motion studies*. In: D'Amico S. (ed), Earthquake Research and Analysis – New Frontiers in Seismology, InTech, pp. 87-140, doi: 10.5772/28189.

Kirkpatrick S., Gelatt C.D. Jr. and Vecchi M.P.; 1983: *Optimization by simulated annealing.* Science, 220, 671-680.

Kurnaz T.F., Ramazanoglu S. and Karavul C.; 2011: *Urban microzonation study for Esenler district, Istanbul, Turkey.* Int. J. Phys. Sci., 6, 4933-4946, doi: 10.5897/IJPS11.604.

Newton C. and Snieder R.; 2012: *Estimating intrinsic attenuation of a building using deconvolution interferometry and time reversal*. Bull. Seismol. Soc. Am., 102, 2200-2208.

O'Connell R.J. and Budiansky B.; 1977: *Viscoelastic properties of fluid-saturated cracked solids.* J. Geophys. Res., 82, 5719-5735.

Paasschens J.C.J.; 1997: *Solution of the time-dependent Boltzmann equation*. Phys. Rev. E, 56, 1135-1141.

Parolai S., Bindi D., Ansal A., Kurtulus A., Strollo A. and Zschau J.; 2010: *Determination of shallow S-wave attenuation by down-hole waveform deconvolution: a case study in Istanbul (Turkey)*. Geophys. J. Int., 181, 1147-1158, doi: 10.1111/j.1365-246X.2010.04567.x.

Petrovic B., Dikmen S.U. and Parolai S.; 2018a: *Real data and numerical simulations-based approaches for estimating the dynamic characteristics of a tunnel formwork building*. Bull. Earthq. Eng., 16, 1633-1656.

Petrovic B., Parolai S., Pianese G., Dikmen S.U., Moldobekov B., Orunbaev S. and Paolucci R.; 2018b: *Joint deconvolution of building and downhole seismic recordings: an application to three test cases*. Bull. Earthq. Eng., 16, 613-641, doi: 10.1007/s10518-017-0215-6.

Picozzi M. and the SAFER and EDIM working groups; 2009a: *The self-organising seismic early warning information network (SOSEWIN).* Geophys. Res. Abstr., 11, EGU2009-8960.

Picozzi M., Strollo A., Parolai S., Durukal E., Özel O., Karabulut S., Zschau J. and Erdik M.; 2009b: *Site characterization by seismic noise in Istanbul, Turkey.* Soil Dyn. Earthq. Eng., 29, 469-482, doi: 10.1016/j.soildyn.2008.05.007.

Rachman A.N., Chung T.W. and Chung K.H.; 2017: *Multiple lapse time window analysis using solely single events in South Korea*. Explor. Geophys., 48, 504-511.

Sato H., Fehler M.C. and Maeda T.; 2012: *Seismic wave propagation and scattering in the heterogeneous Earth. 2nd ed.* Springer, Berlin-Heidelberg, 496 pp., doi: 10.1007/978-3-642-23029-5.

Snieder R. and Şafak E.; 2006: *Extracting the building response using seismic interferometry: theory and application to the Millikan Library in Pasadena, California.* Bull. Seismol. Soc. Am., 96, 586-598, doi: 10.1785/0120050109.

Sørensen M.B., Oprsal I., Bonnefoy-Claudet S., Atakan K., Mai P.M., Pulido N. and Yalciner C.; 2006: *Local site effects in Ataköy, Istanbul, Turkey, due to a future large earthquake in the Marmara Sea*. Geophys. J. Int., 167, 1413-1424, doi: 10.1111/j.1365-246X.2006.03204.x.

Tamura Y., Yoshida A. and Zhang L.; 2004: *Evaluation techniques of damping in buildings*. In: Proc. CTBUH 2004 Seoul Conference, Seoul, South Korea, pp. 158-165.

Zeng Y., Su F. and Aki K.; 1991: *Scattering wave energy propagation in a random isotropic scattering medium: 1. Theory.* J. Geophys. Res., 96, 607-619.

Corresponding author: Melese Temesgen Salilih
Centre for Seismological Research
National Institute of Oceanography and Applied Geophysics - OGS
Via Treviso 55, 33100 Udine, Italy
Phone: +39 338 140 9080; e-mail: melesesalilih@gmail.com